

Magnetoelasticity of $\text{Co}_{25}\text{Fe}_{75}$ thin films

Cite as: J. Appl. Phys. **126**, 103902 (2019); <https://doi.org/10.1063/1.5116314>

Submitted: 25 June 2019 . Accepted: 20 August 2019 . Published Online: 09 September 2019

Daniel Schwienbacher , Matthias Pernpeintner, Lukas Liensberger, Eric R. J. Edwards, Hans T. Nembach, Justin M. Shaw, Mathias Weiler , Rudolf Gross , and Hans Huebl

COLLECTIONS

 This paper was selected as an Editor's Pick



View Online



Export Citation



CrossMark

ARTICLES YOU MAY BE INTERESTED IN

[High spin-wave propagation length consistent with low damping in a metallic ferromagnet](#)
Applied Physics Letters **115**, 122402 (2019); <https://doi.org/10.1063/1.5102132>

[Efficient computation of demagnetizing fields for magnetic multilayers using multilayered convolution](#)

Journal of Applied Physics **126**, 103903 (2019); <https://doi.org/10.1063/1.5116754>

[Impact of Dzyaloshinskii-Moriya interactions on the thermal stability factor of heavy metal/magnetic metal/oxide based nano-pillars](#)

Journal of Applied Physics **126**, 103905 (2019); <https://doi.org/10.1063/1.5109484>

Lock-in Amplifiers
up to 600 MHz



Watch



Magnetoelasticity of $\text{Co}_{25}\text{Fe}_{75}$ thin films



Cite as: J. Appl. Phys. **126**, 103902 (2019); doi: [10.1063/1.5116314](https://doi.org/10.1063/1.5116314)

Submitted: 25 June 2019 · Accepted: 20 August 2019 ·

Published Online: 9 September 2019



Daniel Schwienbacher,^{1,2,3,a)} Matthias Pernpeintner,^{1,2} Lukas Liensberger,^{1,2} Eric R. J. Edwards,⁴ Hans T. Nembach,⁴ Justin M. Shaw,⁴ Mathias Weiler,^{1,2} Rudolf Gross,^{1,2,3} and Hans Huebl^{1,2,3,b)}

AFFILIATIONS

¹Walther-Meissner-Institut, Bayerische Akademie der Wissenschaften, Walther Meissner Str. 8, 85748 Garching, Germany

²Technische Universität München, James-Franck-Str. 1, 85748 Garching, Germany

³Munich Center for Quantum Science and Technology (MCQST), Schellingstraße 4, 80799 München, Germany

⁴National Institute of Standards and Technology, Boulder, Colorado 80305, USA

a) daniel.schwienbacher@wmi.badw.de

b) huebl@wmi.badw.de

ABSTRACT

We investigate the magnetoelastic properties of $\text{Co}_{25}\text{Fe}_{75}$ and $\text{Co}_{10}\text{Fe}_{90}$ thin films by measuring the mechanical properties of a doubly clamped string resonator covered with multilayer stacks containing these films. For the magnetostrictive constants, we find $\lambda_{\text{Co}_{25}\text{Fe}_{75}} = (-20.68 \pm 0.25) \times 10^{-6}$ and $\lambda_{\text{Co}_{10}\text{Fe}_{90}} = (-9.80 \pm 0.12) \times 10^{-6}$ at room temperature, in contrast to the positive magnetostriction previously found in bulk CoFe crystals. $\text{Co}_{25}\text{Fe}_{75}$ thin films unite low damping and sizable magnetostriction and are thus a prime candidate for micromechanical magnonic applications, such as sensors and hybrid phonon-magnon systems.

Published under license by AIP Publishing. <https://doi.org/10.1063/1.5116314>

I. INTRODUCTION

Magnetic alloys are an extremely well studied material group due to their importance for applications in magnetic information storage. While properties such as saturation magnetization and magnetic anisotropy play key roles in the static configuration and stability of the magnetization state, material parameters related to magnetization control (beyond such enacted by static magnetic fields) are also of interest. Apart from current-induced magnetization switching,^{1–5} techniques based on magnetostriction constitute a complementary way to control the magnetization direction. Here, the elastic deformation of the material generates a strain-induced anisotropy term which can be used to reorient the magnetization. Static control^{6–9} as well as the excitation of magnetization dynamics^{10–13} has already been demonstrated. Moreover, the reciprocal effect is used in sensing applications based on magnetoelastics.¹⁴

Cobalt iron alloys recently regained interest as an electrically conducting ferromagnetic material with ultralow damping.^{15–17} Damping in thin film $\text{Co}_{25}\text{Fe}_{75}$ was found to be as low as in thin film yttrium iron garnet.¹⁸ Since applications in spin electronics are usually based on thin films, quantification of the magnetoelastic properties of thin film $\text{Co}_{25}\text{Fe}_{75}$ is required. In previous studies,^{19–31} only bulk materials have been studied.

In this article, we investigate the magnetostrictive properties of $\text{Co}_{25}\text{Fe}_{75}$ and $\text{Co}_{10}\text{Fe}_{90}$ thin films (10/20 nm). The films were grown using the same recipe as the ultralow damping material of Ref. 15. In our study, we employ magnetostriction measurements based on nanostrings as reported in Ref. 32. The paper is organized as follows: First, we briefly sketch the physics of the nanostrings and how it is influenced by the magnetoelastic properties of the $\text{Co}_x\text{Fe}_{1-x}$ thin films deposited on them. Then, we give a short description of sample fabrication and the experimental setup used to characterize them. We then provide an in-depth data analysis and summarize our findings.

II. MODEL AND MEASUREMENT CONCEPT

To access the magnetostrictive properties of thin film $\text{Co}_x\text{Fe}_{1-x}$, we deposit the ultralow magnetization damping layer stacks reported in Ref. 15 onto a doubly clamped, suspended silicon nitride string (cf. Figure 1). The resonance frequency of this multilayer string scales approximately with $1/L\sqrt{\sigma_{\text{eff}}/\rho_{\text{eff}}}$, where L is the length of the string, σ_{eff} is the effective stress along the string, and ρ_{eff} is the effective mass density of the whole layer stack. σ_{eff} is directly related to the static stress σ_0 in the system. Moreover, when we measure the resonance frequency as a function of the magnetization direction, we

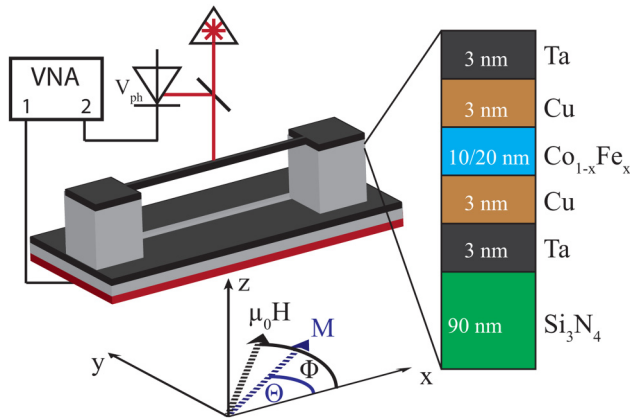


FIG. 1. Schematic of doubly clamped Si₃N₄ nanostring covered with a CoFe layer stack on top (black) and an interferometric readout setup. The string is supported by posts etched from the silicon substrate (grey). The whole sample is mounted on a piezoactuator (red). Φ is the angle between the external magnetic field and the x -direction (along the string), and Θ denotes the angle between the x -direction and the magnetization direction in the CoFe film. The layer stack with Ta(3 nm) and Cu(3 nm) seed and capping layers is the same as used in Ref. 15. The CoFe layer thickness varied for different alloy ratios. To extract the resonance frequency of the oop mechanical motion of the string, the amplitude of a reflected laser beam is measured with a photodiode and analyzed with a VNA.

expect a modulation of the resonance frequency because the magnetoelastic interaction changes the stress in the sample depending on the magnetization direction. In more detail, the resonance frequency of a highly tensile stressed, doubly clamped nanostring, also depends on material parameters, like Young’s modulus E , and size dependent parameters like the string moment of inertia I and its cross section $A = wt$, where w is the string’s width and t its thickness. A nanostring can be treated as highly tensile stressed, if the static stress σ_0 is the dominant parameter $[(4Ew^2t^4\rho\Omega_0^2)/12 \ll \sigma_0^2(wt)^2]$. The magnetization direction dependent resonance frequency of the string is given by^{33,34}

$$\Omega_0 = \frac{(\sigma_0 + \sigma_1 \cos \Theta^2)\pi\sqrt{\rho_{\text{eff}}^{-1}}}{L\sqrt{\sigma_0 + \sigma_1 \cos \Theta^2 - 2\sqrt{Et^2/12}}}. \quad (1)$$

This equation includes geometry sensitive bending effects to first order (cf. Appendix A). The magnetization orientation with respect to the long axis of the string is denoted by Θ , and σ_1 determines the change in stress along the x -direction. Note, however, that Θ is not directly accessible in our experiment. Our data are rather recorded as a function of the applied magnetic field direction, which is given by the angle Φ (see Fig. 1). To relate Φ to Θ , we calculate the magnetization direction Θ for a given external magnetic field \mathbf{H} by using a free energy minimization approach. For a uniaxial anisotropy along x , we obtain

$$\Theta(\Phi) = \Phi - \frac{K\sin(2\Phi)}{-M_S\mu_0 H + 2K\cos(2\Phi)}, \quad (2)$$

with the saturation magnetization M_S and the uniaxial anisotropy constant K .³⁵

With relation (2), we can translate the measured $\Omega_0(\Phi)$ dependence into an $\Omega_0(\Theta)$ dependence, which is fitted by Eq. (1) to derive the stress component σ_1 . The derived value of σ_1 finally allows us to determine the magnetostrictive constant,³²

$$\lambda_{\parallel} = \frac{\sigma_1 t}{t_{\text{CoFe}} E_{\text{CoFe}}}. \quad (3)$$

Note that due to the specific geometry of the string, we can access only the parallel part ($\lambda_{\parallel} \parallel x$) of the magnetostrictive constant, because only stress variations in the x -direction change the string’s resonance frequency. The quantity λ_{\parallel} used here is equivalent to the quantity λ_S commonly used for polycrystalline material in the literature.³⁶ From this magnetostrictive constant, we can calculate the magnetoelastic constant b ,^{10,36}

$$b = \frac{B}{M_S} = -\frac{3\lambda_{\parallel} G}{M_S}, \quad (4)$$

with shear modulus G of the CoFe alloy.

III. SAMPLE PREPARATION

For the fabrication of the freely suspended Co_xFe_{1-x} layers on top of silicon nitride string resonators, we start with a single crystalline silicon wafer, which is commercially coated with a $t_{\text{SiN}} = 90$ nm thick, highly tensile-stressed, low pressure chemical vapor deposition (LPCVD) grown Si₃N₄ (SiN) film. Note that SiN is an established substrate material for torque magnetometry.^{44,45} We define the geometry of the strings by defining a metal etch mask using electron beam lithography, electron beam evaporation of aluminum, and a lift-off process. The pattern is transferred to the silicon nitride using an anisotropic reactive ion etching (RIE) process to define the SiN strings. Subsequently, a second isotropic RIE process is used to remove the Si substrate below the strings to release them and enable mechanical in-plane (ip) and out-of-plane (oop) motion. The Al etching mask is removed afterwards. The resulting unloaded SiN strings show typical Q -factors of about 15000 for the ip and oop fundamental modes. As the last fabrication step, a Ta/Cu/CoFe/Cu/Ta layer stack (as shown in Fig. 1) was deposited on top of the strings by magnetron sputtering. Thus, the CoFe stack covers the strings as well as the surrounding substrate. However, we ensure that there is no mechanical contact between the top- or string layer and the substrate level. We investigate two sets of strings with two different CoFe alloys: The reported ultralow damping Co₂₅Fe₇₅, and Co₁₀Fe₉₀ as an alloy with larger damping for comparison. For each Co-Fe alloy, we investigate the mechanical response for different string lengths L (25 μm , 35 μm , and 50 μm) and string widths w (150 nm and 200 nm). We suspect that during the sputtering process, materials were also deposited on the sides of the string, creating an overhang.

To measure the resonance frequencies of the strings, we use a free space optical interferometer similar to the setup in Ref. 32 (see Fig. 1). A laser beam with a wavelength of 633 nm is focused on the center of the string ($x = L/2$) and interferometry is used to measure the displacement of the nanostring’s oop motion. To

excite this mode at its resonance frequency, the entire sample is glued on an extended piezoactuator using a novolak polymer (Fig. 1, red layer). The resonance frequency of the string is obtained by measuring the output voltage of a photodiode while sweeping the drive frequency using a vector network analyzer (VNA). The drive voltage is chosen small enough to keep the piezoactuator as well as the strings in their respective linear regimes. The sample holder is mounted on a xyz piezo stage to allow positioning and focusing of the laser spot on an individual string. The interferometer is operated at room temperature. The sample stage is placed in vacuum ($p < 0.01$ Pa) to prevent air damping. To control the magnetization, and, in particular, the magnetization orientation of the Co-Fe on the string, the sample is positioned between the pole pieces of an electromagnet. The applied field direction is varied by rotating the electromagnet, whereas the sample position and orientation remain fixed.

IV. DATA ANALYSIS

Figure 2(a) shows a color-encoded plot of the mechanical response function as a function of actuation frequency and applied magnetic field direction. Red highlights large oop mechanical displacement, while blue indicates no visible motion. The raw data are measured for a constant actuation amplitude and a fixed magnitude of the magnetic field $\mu_0 H = 950$ mT. The resonance frequency of the string is 180° periodic with respect to the external magnetic field direction. A cut of this dataset at $\Phi = 153^\circ$ is displayed in the inset of Fig. 2(b), showing the mechanical response as a function of the drive frequency. As the sample position is not actively stabilized, we attribute variations in the detected amplitude to drifts in the optical alignment originating from the rotation of the magnetic field direction. We estimate typical displacement amplitudes present in our experiment to be in the nanometer range.³⁷ To extract the resonance frequency, we fit a Lorentzian line shape to the data for each measured angle Φ . From this fit, we find a linewidth (full-width at half-maximum) of 900 Hz corresponding to a Q -factor of the string of about 8000. This Q -factor is significantly smaller than that of a pure SiN string and can mainly be attributed to the added metal layer stack. The stack increases the overall mass of the string, and thereby its effective density, which lowers the resonance frequency [see Eq. (1)]. Moreover, adding a metal component is known to change the mechanical damping of nanostrings.^{38,39}

Figure 2(b) shows the evolution of the resonance frequency as a function of Φ . For comparison, we have measured a set of strings with different lengths and widths. To analyze our data, we use a global fit routine employing Eqs. (1) and (2). The fit uses the data of all strings for each CoFe composition as an input parameter. In addition, we use the thickness of $t = 112$ nm of the nanostring and an effective density of $\rho_{\text{eff}} = 4350$ kg/m³ of each string as fixed parameters, as both are known fabrication parameters. The thickness of the metal stack was determined by calibrating the deposition rates using x-ray reflectometry. The density was calculated by using the weighted average of the single material bulk densities.⁴⁰ Figure 3 shows the fit of Ω_0 for the Co₂₅Fe₇₅ compound for strings of different lengths. Here, the prestress σ_0 , the magnetically induced stress σ_1 , and Young's modulus E of the sample were set as global fit parameters. For the fit, we used fixed values for the length

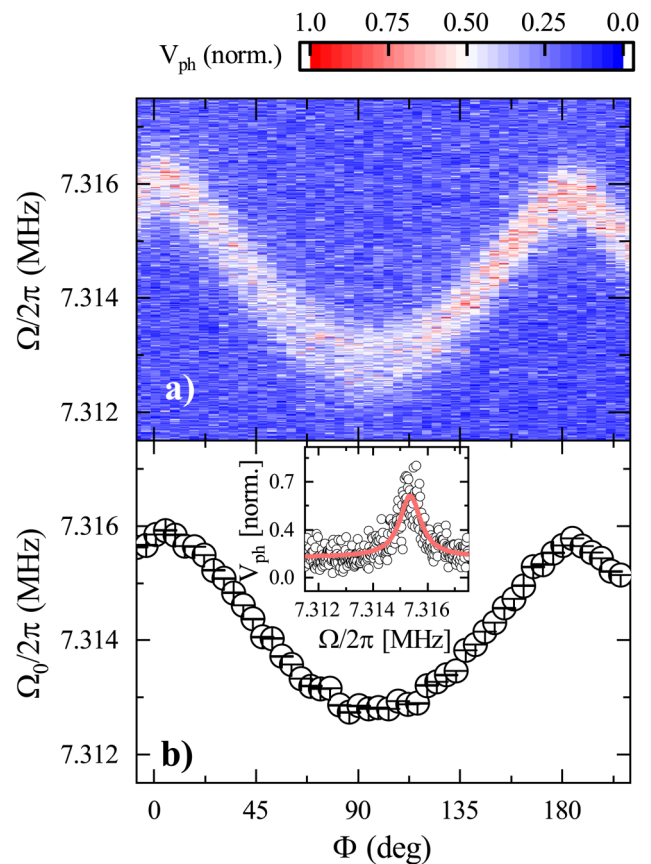


FIG. 2. Mechanical response of the fundamental mode of a $25\ \mu\text{m}$ long nanostring as a function of external field direction Φ at $\mu_0 H = 950$ mT. (a) shows the frequency dependent photovoltage as a function of external magnetic field direction and drive frequency, this is a direct measure for the mechanical amplitude of the string. (b) shows the extracted resonance frequencies at specific field directions. The inset in (b) shows a slice from (a) at $\Phi = 153^\circ$ and the fit to a Lorentzian line shape (red line) used to extract the resonance frequency. Error bars are fit errors.

L of the strings with $25\ \mu\text{m}$ and $35\ \mu\text{m}$. The string lengths of the two nominally $50\ \mu\text{m}$ long strings are free fit parameters. This allows us to account for small variations in the frequencies of the two nominally identical strings, which otherwise should have exactly the same frequency. The fitted lengths are $51.2\ \mu\text{m}$ and $50.8\ \mu\text{m}$ in good agreement with the design value of $50\ \mu\text{m}$. The uniaxial anisotropy constant K is a free fit parameter for each string, as it might differ from string to string. As shown in Fig. 3(a), we find good agreement between the global fit and the data using $\sigma_1 = -386 \pm 5$ kPa, $\sigma_0 = 458.7 \pm 0.1$ MPa, and $E = 857.7 \pm 0.2$ GPa. The extracted prestress is reduced compared to the prestress in a SiN string without any metal on top. This can be attributed to a compressive stress in the layer stack of $\Delta\sigma_0 \approx 270$ MPa. The sputtering process may change the prestress of the composite string. Even though the sputtering process is carried out at room temperature, the temperature of the nanostring is expected to increase significantly due to the

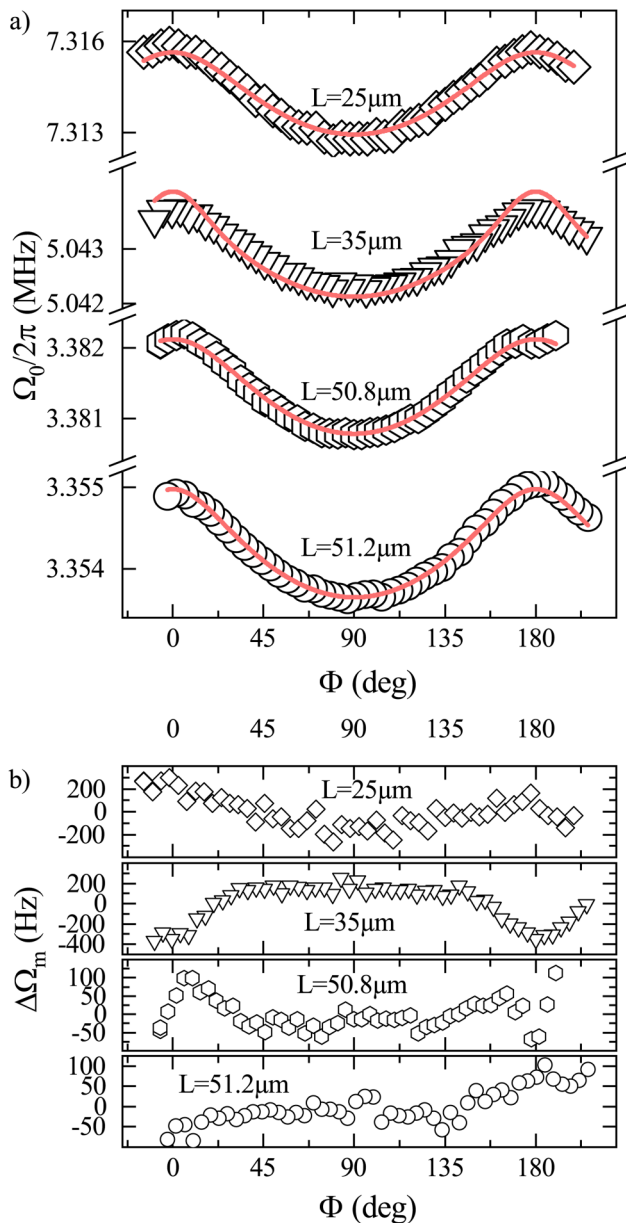


FIG. 3. Global fit to magnetization direction dependent resonance frequencies of strings with different lengths covered with the $\text{Co}_{25}\text{Fe}_{75}$ stack. The resonance frequencies of the strings with a length of $25\ \mu\text{m}$ (diamonds), $35\ \mu\text{m}$ (triangles), $50.8\ \mu\text{m}$ (hexagons), and $51.2\ \mu\text{m}$ (circles) length were globally fit using Eqs. (1) and (2) (red lines). Fit errors are within the size of the data symbols. In (b), the deviation $\Delta\Omega_m = \Omega_0 - \Omega_{\text{fit}}$ is plotted vs Φ . The residuals are nonzero for all the strings; however, no clear systematics are apparent.

poor thermal coupling of the string to the substrate. Thus, the metal stack is deposited at a temperature well above room temperature. Cooling down the string coated by the metal stack after deposition then results in a partial compensation of the prestress due to

different thermal expansion coefficients of SiN and the metal stack. A temperature increase of about 300 K could explain the observed change of prestress. Also, the extracted Young's modulus is larger than expected from Young's moduli of the individual materials.⁴⁰ Using (3) and (4) in combination with the known sample parameters and the Co-Fe Young's modulus, we obtain a $\lambda_{\parallel} = (-20.68 \pm 0.25) \times 10^{-6}$ and $b = 2.62 \pm 0.05\ \text{T}$ for $\text{Co}_{25}\text{Fe}_{75}$. We obtain these values when considering $t_{\text{CoFe}} = 10\ \text{nm}$, $t = 112\ \text{nm}$, $E_{\text{CoFe}} = 208\ \text{GPa}$,⁴⁰ $M_S = 1.904\ \text{MA m}^{-1}$,¹⁶ as well as the shear modulus $G = 81.7\ \text{GPa}$.⁴⁰ Here, Young's modulus and shear modulus for $\text{Co}_{25}\text{Fe}_{75}$ were calculated from the literature values of the single materials.

In addition, the measured data allow us to access magnetic anisotropy parameters. We find an anisotropy $2K/M_S \approx 300\ \text{mT}$ with an easy axis pointing along the y -direction of the string. Note that because we have access only to in-plane measurements, we can calculate only projections of an anisotropy to the x - y -plane of the sample. Combined with the calculated shape anisotropy $B_{\text{shape}} \approx 100\ \text{mT}$,³⁵ with an easy axis along the x -direction of the string, the total anisotropy field in the sample adds up to $B_{\text{aniso}} \approx 400\ \text{mT}$. The compressive stress in the metal $\Delta\sigma_0$ leads to a magnetoelastic anisotropy of $B_{\text{magnet}} \approx 4\ \text{mT}$.³⁶ Unfortunately, we cannot identify the origin of the anisotropy. However, we speculate that the overhanging material at the edges of the string might result in a preferential orientation of the magnetization direction perpendicular to the string. The deviation $\Delta\Omega_m = \Omega_0 - \Omega_{\text{fit}}$ shown in Fig. 3(b) shows that there is some disagreement between the model and the data, however, without any systematics. Deviations are lower for the two strings where the string length is a fit parameter, compared to the other strings where the string length was fixed for the fit. In addition, we note that the assumption of a single uniaxial anisotropy in the system may lead to increased systematic uncertainties.

V. DISCUSSION

To set these results in context, we plot the extracted values of λ_{\parallel} and b for the two measured thin film CoFe alloys ($\text{Co}_{25}\text{Fe}_{75}$ and $\text{Co}_{10}\text{Fe}_{90}$) as well as the values for thin-film Co³² and bulk Fe⁴⁰ in Fig. 4. The ultralow damping material investigated in this work seems to follow the simple trend of an interpolating magnetostrictive constant connecting the bulk values. Since the values for the saturation magnetization and shear modulus are similar for Co and Fe, the b is approximately linearly proportional to λ . Nevertheless, Fig. 4 also shows the data from Hunter *et al.*²⁰ (star with dot) obtained using a cantilever displacement method on various 500 nm thick $\text{Co}_x\text{Fe}_{1-x}$ films. Their data show an entirely different behavior, most importantly an opposing sign of $\lambda_S \approx 50 \times 10^{-6}$. Even earlier experiments by Hall¹⁹ (stars) extrapolated an in-plane magnetostrictive constant of $\lambda_{100} \approx 75 \times 10^{-6}$ for $\text{Co}_{25}\text{Fe}_{75}$ and $\lambda_{100} \approx 48 \times 10^{-6}$ for $\text{Co}_{10}\text{Fe}_{90}$ for bulk crystal discs. We note, however, that the seed layer material, interface effects between the seed and the CoFe layer, and the sputtering conditions are crucial for the realization of ultralow damping material.⁴¹ Thus, we rationalize that the magnetoelastic properties can be significantly altered due to interface effects. Low damping $\text{Co}_{25}\text{Fe}_{75}$ was realized on SiO_x ⁴¹ and Si ¹⁶ using the same seed layers used in this work. To ensure that the low-damping behavior of the Co-Fe is still present when changing

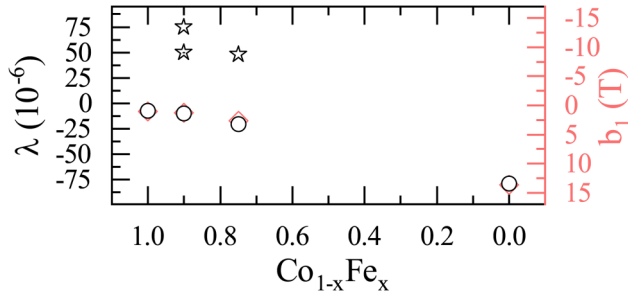


FIG. 4. Magnetostrictive and magnetoelastic constants for the two $\text{Co}_{1-x}\text{Fe}_x$ alloys and pure metals (Co^{32} and Fe^{40}) for reference. Circles show the magnetostrictive constant (λ_{\parallel}) on the left scale, while diamonds (red) depict the corresponding magnetoelastic constant (b) on the right scale. The star shaped data points correspond to literature values from Refs. 19 and 20. Uncertainties in the alloy composition ($\pm 2\%$) are represented by the symbol size for the $\text{Co}_{25}\text{Fe}_{75}$ and $\text{Co}_{10}\text{Fe}_{90}$ compounds, uncertainties in the values of λ_{\parallel} and b are given in the text.

the substrate from Si^{15} to SiN used in this paper, we performed ferromagnetic resonance (FMR) experiments on unpatterned CoFe -stacks on SiN samples (cf. Appendix C) and find an oop Gilbert damping of $\alpha = (2.1 \pm 0.1) \times 10^{-3}$ for a 10 nm thick $\text{Co}_{25}\text{Fe}_{75}$ film which is in agreement with the values from Schoen *et al.*¹⁵

VI. SUMMARY

In this article, we extract the magnetostrictive constants of two low magnetic damping Co-Fe alloys grown within a layer stack.¹⁵ To get a quantitative value for the magnetostriction, we use a magnetization direction dependent resonance frequency measurement of a nanostring,³² which is covered with the magnetostrictive layer stack. This method allows the investigation of the magnetostrictive and elastic properties of thin film magnetic layers, even with small sample volumes and high aspect ratios, both of which are requisites for future technical applications of spintronic devices including sensing applications. We extract a magnetostrictive constant of $\lambda_{\parallel} = (-20.72 \pm 0.33) \times 10^{-6}$, which corresponds to a magnetoelastic constant of $b = 2.62 \pm 0.05 \text{ T}$ for the ultralow damping $\text{Co}_{25}\text{Fe}_{75}$ compound, as well as $\lambda_{\parallel} = (-9.8 \pm 0.12) \times 10^{-6}$ and $b = 1.3 \pm 0.02 \text{ T}$ for the $\text{Co}_{10}\text{Fe}_{90}$ compound. This shows that the magnetoelastic properties of the two investigated alloys have the same order of magnitude as the constituent materials but differ significantly between the low-damping and the normal damping case. Thus, CoFe and, in particular, the ultralow damping compound $\text{Co}_{25}\text{Fe}_{75}$ show a sizeable magnetoelastic constant and hereby make an ideal candidate for sensing and magnetization dynamic applications which rely on low damping materials.

See Appendixes for the derivation of Eq. (1) and the reference broadband ferromagnetic resonance measurements of thin film CoFe grown on the SiN substrate.

ACKNOWLEDGMENTS

This work was funded by the Deutsche Forschungsgemeinschaft (DFG, German Research Foundation) under Germany's Excellence Strategy—EXC-2111-390814868 and Project No. WE5386/4-1.

APPENDIX A: DERIVATION OF THE RESONANCE FREQUENCY OF A TENSILE STRESSED STRING RESONATOR CONSIDERING THE BENDING AT THE CLAMPS

The resonance frequency of a highly tensile stressed string (HTS) resonator is given by^{34,32}

$$\Omega_{n,\text{HTS}} = \frac{n\pi}{L} \sqrt{\frac{\sigma_0}{\rho}}, \quad (\text{A1})$$

where n is the mode index, L is the length of the string, σ_0 is the tensile stress of the material, and ρ its density. This formula assumes that the additional energy due to a displacement is only stored in the stress of the string, i.e., it neglects the bending of the material and the stored energy. In the following, we discuss the effect of bending on the resonance frequency of the string to first order. The derivation follows the discussion in Ref. 42.

We start using the Euler-Bernoulli beam theory for a pre-stressed prismatic beam with cross section $A = wt$, where w is the string's width and t its thickness. Considering a restoring force based on the bending of the string and the change in the stress $dF_{\text{restoring}} = dF_{\text{bending}} + dF_{\text{prestress}}$, we obtain the equation of motion for the transverse vibrational mode of the infinitesimal volume element of the beam,^{33,43}

$$-EI \frac{\partial^4 v}{\partial x^4} + \sigma_0 A \frac{\partial^2 v}{\partial x^2} = \rho A \frac{\partial^2 v}{\partial t^2}, \quad (\text{A2})$$

with EI being the flexural rigidity composed of Young's modulus E and the moment of inertia I . If we assume a harmonic time dependence for the local displacement $v(x, t) = v(x)\exp(-i\Omega t)$,³³ the differential equation transforms to

$$-EIv^{(4)}(x) + \sigma_0 Av^{(2)}(x) = -\rho A \Omega^2 v(x). \quad (\text{A3})$$

The general solution for Eq. (A3) is given by^{33,43}

$$v(x) = c_1 \exp(\alpha x) + c_2 \exp(-\alpha x) + c_3 \sin(\beta x) + c_4 \cos(-\beta x), \quad (\text{A4})$$

with

$$\alpha = \sqrt{\mu_+} > 0 \quad (\text{A5})$$

and

$$\beta = -i\sqrt{\mu_-} > 0, \quad (\text{A6})$$

$$I = \frac{wt^3}{12}, \quad (\text{A7})$$

$$A = wt, \quad (\text{A8})$$

$$\mu_{\pm} = \frac{\sigma_0 A \pm \sqrt{\sigma_0^2 A^2 + EI \rho A \Omega^2}}{2EI}. \quad (\text{A9})$$

For a doubly clamped beam, the boundary conditions are

given by^{43,33}

$$\begin{aligned} v(x = \pm L/2) &= 0, \\ \partial v(x = \pm L/2)/\partial x &= 0. \end{aligned} \tag{A10}$$

The application of these boundary conditions to the general solution (A4) results in a homogeneous system of four linear equations and four variables c_i ($i = 1, 2, 3, 4$). Nontrivial solutions for the displacement are given by a vanishing determinant of this system:

$$\begin{aligned} e^{-\alpha L}[(\alpha^2 - \beta^2)(e^{2\alpha L} - 1)\sin(\beta L) \\ + 4\alpha\beta/(e^{2\alpha L} + 1)\cos(\beta L)] = 0. \end{aligned} \tag{A11}$$

While the above result is general, we want to focus next on suitable approximations for our problem. For our tensile stressed (TS) nanostrings, $4EI\rho A\Omega^2 \ll \sigma_0^2 A^2$. In this case, we can expand the square root in (A9) to the first order

$$\mu_{\pm} \approx \frac{\sigma_0 A}{2EI} \left[1 \pm \left(1 + \frac{2EI\rho A\Omega^2}{\sigma_0^2 A^2} \right) \right]. \tag{A12}$$

Combining (A12) with (A5) and (A8), we obtain

$$\alpha \approx \alpha_0 := \sqrt{\frac{\sigma_0 A}{EI}} \tag{A13}$$

and

$$\beta \approx \sqrt{\frac{\rho}{\sigma_0}} \Omega. \tag{A14}$$

Next, we substitute the HTS approximation Eq. (A1) into Eq. (A14) and obtain

$$\beta L = \sqrt{\frac{\rho}{\sigma_0}} \Omega_{n,HTS} L \approx \pi n. \tag{A15}$$

Therefore,

$$\cos(\beta L) \approx (-1)^n.$$

This simplifies Eq. (A11) to

$$\begin{aligned} (\alpha_0^2 - \beta^2)(e^{2\alpha_0 L} - 1)\sin(\beta L) \\ + 2\alpha_0\beta[2e^{\alpha_0 L} - (-1)^n e^{2\alpha_0 L} + (-1)^n] = 0. \end{aligned} \tag{A16}$$

For the geometries discussed in this work, which are $L \approx 50 \mu\text{m}$, $t \approx w \approx 100 \text{ nm}$ (see also Sec. III) and material parameters,^{40,32} we find $\alpha_0 > 10\beta$ with $\beta L \approx n\pi > 1$. Thus, $e^{\alpha_0 L} \gg 1$. Under these conditions, (A16) reduces to

$$(\alpha_0^2 - \beta^2)\sin(\beta L) - (-1)^n 2\alpha_0\beta = 0.$$

Using $\alpha_0 \gg \beta$, we obtain

$$\alpha_0 \sin(\beta L) - (-1)^n 2\beta = 0. \tag{A17}$$

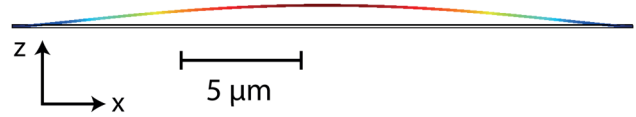


FIG. 5. Result of a numeric finite element simulation of the eigenfrequency and mode shape of a $L = 25 \mu\text{m}$ nanostring, alike to what is shown in Fig. 2. Using the same material and geometry parameters as in the experiment, as well as the experimentally obtained prestress ($\sigma_0 = 458 \text{ MPa}$), the resonance frequency and the mode shape were simulated. Giving a resonance frequency of $\Omega_{\text{simu}} = 7.373 \text{ MHz}$ and the mode-shape of an undisturbed oop oscillation.

Next, we solve for β by using (A15) and expanding $\sin(\beta L)$ around $n\pi$:

$$\sin(\beta L) \approx (-1)^n (\beta L - n\pi). \tag{A18}$$

Substituting this into Eq. (A17), we obtain

$$\beta = \frac{n\alpha_0\pi}{\alpha_0 L - 2}. \tag{A19}$$

As the last step, we identify α_0 and β using Eqs. (A13) and (A14) with the geometry parameters of the resonator and the resonance frequency $\Omega_n/2\pi$. We obtain

$$\Omega_{n,TS} = \frac{n\sigma_0\pi\sqrt{A/\rho}}{\sqrt{\sigma_0 AL - 2\sqrt{EI}}} = \Omega_{n,HTS} \frac{\sqrt{\sigma_0 AL}}{\sqrt{\sigma_0 AL - 2\sqrt{EI}}}. \tag{A20}$$

Equation (A20) represents the first order correction accounting for the bending of the resonator. To further include the impact of the magnetoelasticity on the resonance frequency of the system, we adapt this formula using the replacements

$$\rho \rightarrow \rho_{\text{eff}}, \tag{A21}$$

$$\sigma_0 \rightarrow \sigma_0 + \sigma_1 \cos(\Theta)^2. \tag{A22}$$

The stress in the CoFe is separated into a magnetostrictive component $\sigma_{\text{CoFe,mag}} := \sigma_1 \cos(\Theta)^2$ depending on the magnetization direction and a static contribution $\sigma_{\text{CoFe,stat}}$.³² This static part contributes to the prestress in the string which is redefined as $\sigma_0 = \sigma_{\text{string}} + \sigma_{\text{CoFe,stat}}$. The stress in the string is assumed to be independent from the magnetization direction. SiN is widely used in magnetometry applications^{44,45} and established as nonmagnetic. In the case of the static stress in CoFe being of different signs compared to the prestress in the string, this needs to be taken into account. Finite element simulations (cf. Appendix B) show that we find no buckling of the string for the given geometry and parameters of a thin metal film on a string. Moreover, these simulations show that buckling only results if the compressive forces from the metal significantly exceed the tensile stress of the SiN. Using the moment of inertia of a string oscillating out of plane $I = wt^3/12$,³³

we obtain Eq. (1) in the main text

$$\Omega_{n,TS} = \frac{n(\sigma_0 + \sigma_1 \cos(\Theta))^2 \pi \sqrt{\rho_{\text{eff}}^{-1}}}{\sqrt{(\sigma_0 + \sigma_1 \cos(\Theta))^2 L - 2\sqrt{Et^2/12}}}, \quad (\text{A23})$$

which is used for the global fit discussed in Sec. V.

APPENDIX B: FINITE ELEMENT SIMULATIONS TO DETERMINE THE MECHANICAL MODE SHAPE

We used a finite element simulation (COMSOL[®]) to simulate the eigenfrequency and mode-shape of a $L = 25 \mu\text{m}$ nanosting. For this simulation, we used the geometry and material parameters of the string shown in Fig. 2. We also assumed an average prestress of the string of 458 MPa, as obtained by our measurements. From this, we find the first eigenfrequency to be $\Omega_{\text{simu}}/2\pi = 7.373 \text{ MHz}$ which is in good agreement with the measured value of 7.316 MHz shown in Fig. 2. The simulation also shows that this eigenfrequency has the mode-shape of a undisturbed out-of-plane oscillation (Fig. 5). This mode-shape also persists for a large range of compressive stresses in the metal film, assuming a tensile prestress in the SiN. Simulations show that the mode shape changes once the compressive stress in the metal significantly exceeds the tensile prestress in the SiN. For a typical prestress of $\sigma_0 \approx 750 \text{ MPa}$, this happens if the compressive stress in the thin metal film reaches $\approx 3400 \text{ MPa}$.

APPENDIX C: MAGNETIZATION DAMPING OF COFE STACKS ON SiN SUBSTRATES MEASURED USING BROADBAND MAGNETIC RESONANCE

We perform broadband ferromagnetic resonance measurements (bbFMR) to investigate the magnetization damping properties of extended CoFe thin films on reference SiN substrates at room temperature.⁴⁶ The continuous CoFe films were grown on Si_3N_4 (SiN) in the same process as the string samples investigated in the main text. The bbFMR measurements were performed as described in Refs. 46 and 47. For the bbFMR, the CoFe layer faced the center conductor of the coplanar waveguide (center conductor width $\approx 250 \mu\text{m}$), which was located between the pole pieces of an electromagnet. A static magnetic field of $|\mu_0 H_0| \leq 3 \text{ T}$ was either applied parallel (ip) or perpendicular (oop) to the sample surface. FMR spectra were acquired for various microwave frequencies $f \leq 43.5 \text{ GHz}$ using a microwave diode detection scheme including a lock-in amplifier and microwave frequency modulation [cf. Fig. 6(a)]. In a first step, we fit the FMR data [an example is shown in Fig. 6(b)] to a Lorentzian lineshape to extract the resonance magnetic field H_{res} and linewidth ΔH for each frequency f . Fitting the resonance magnetic field H_{res} vs frequency f [see Figs. 6(c) and 6(e)] to⁴⁶

$$f(H_{\text{res}}^{\text{ip}}) = \frac{|\gamma|}{2\pi} \mu_0 \sqrt{(H_{\text{res}} + H_{\text{aniso}})(H_{\text{res}} + H_{\text{aniso}} + M_{\text{eff}})} \quad (\text{C1})$$

and

$$f(H_{\text{res}}^{\text{oop}}) = \frac{|\gamma|}{2\pi} \mu_0 \cdot (H_{\text{res}} - M_{\text{eff}}), \quad (\text{C2})$$

for ip and oop data, respectively, yields the effective magnetization M_{eff} , the in-plane anisotropy H_{aniso} and the gyromagnetic ratio

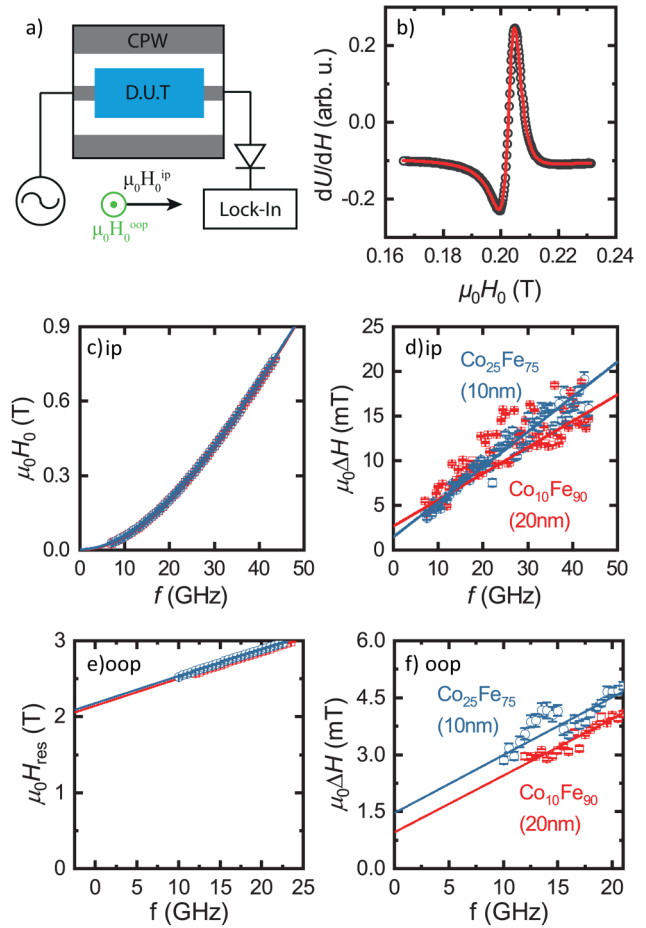


FIG. 6. (a) Sketch of the FMR measurement setup: The sample is positioned on the center conductor of a coplanar waveguide (CPW) with the CoFe facing the CPW. The CPW is connected to a microwave source on one side and to a microwave diode and a lock-in amplifier at the other. An external magnetic field is applied [(c) and (d)] in-plane or [(e) and (f)] out-of-plane. (b) Exemplary field-swept FMR measurement at $f = 20 \text{ GHz}$ for $\text{Co}_{10}\text{Fe}_{90}$ with the external field applied in-plane. Frequency dependence of the ip (oop) resonance field H_{res} [(c) and (e)] and full width half maximum ΔH [(d) and (f)] of the FMR spectra obtained from 20 nm $\text{Co}_{10}\text{Fe}_{90}$ (red) and 10 nm $\text{Co}_{25}\text{Fe}_{75}$ (blue) grown on top of a Si_3N_4 substrate. The solid lines are fits to the data.

$\gamma = g\mu_B/\hbar$. The Gilbert damping was extracted from the linewidth over frequency data [cf. Figs. 6(d) and 6(f)] using⁴⁶

$$\mu_0 \Delta H = \mu_0 \Delta H_0 + \frac{4\pi\alpha f}{|\gamma|}. \quad (\text{C3})$$

The extracted fit values are listed in Table I. All values are in good agreement with the values measured by Schoen *et al.*¹⁵ From this, we conclude that using SiN as a substrate does not change the low damping behavior of the CoFe stack. Note that the extracted α values for the oop field geometry are expected to be better than for the ip

TABLE I. List of the fit values extracted from broadband magnetic resonance measurements shown in Fig. 6.

	$\mu_0 M_{\text{eff}}$ (T)	g	$\mu_0 \Delta H$ (mT)	α (10^{-3})
Co ₁₀ Fe ₉₀ (ip)	2.12 ± 0.01	2.08 ± 0.01	2.6 ± 0.3	4.2 ± 0.2
Co ₂₅ Fe ₇₅ (ip)	2.16 ± 0.01	2.06 ± 0.01	1.4 ± 0.2	5.6 ± 0.2
Co ₁₀ Fe ₉₀ (oop)	2.14 ± 0.01	2.00 ± 0.01	0.95 ± 0.2	2.0 ± 0.1
Co ₂₅ Fe ₇₅ (oop)	2.17 ± 0.01	2.00 ± 0.01	1.4 ± 0.2	2.1 ± 0.1
			$\mu_0 H_{\text{aniso}}$ (mT)	
Co ₁₀ Fe ₉₀ (ip)				-0.8 ± 0.1
Co ₂₅ Fe ₇₅ (ip)				-3 ± 0.1

geometry, as the oop configuration suppresses the two-magnon scattering process.

REFERENCES

- ¹S. Mangin, D. Ravelosona, J. A. Katine, M. J. Carey, B. D. Terris, and E. E. Fullerton, "Current-induced magnetization reversal in nanopillars with perpendicular anisotropy," *Nat. Mater.* **5**, 210–215 (2006).
- ²S. Krause, L. Berbil-Bautista, G. Herzog, M. Bode, and R. Wiesendanger, "Current-induced magnetization switching with a spin-polarized scanning tunneling microscope," *Science* **317**, 1537–1540 (2007).
- ³T. Yang, T. Kimura, and Y. Otani, "Giant spin-accumulation signal and pure spin-current-induced reversible magnetization switching," *Nat. Phys.* **4**, 851–854 (2008).
- ⁴I. M. Miron, K. Garello, G. Gaudin, P.-J. Zermatten, M. V. Costache, S. Auffret, S. Bandiera, B. Rodmacq, A. Schuhl, and P. Gambardella, "Perpendicular switching of a single ferromagnetic layer induced by in-plane current injection," *Nature* **476**, 189–193 (2011).
- ⁵L. Liu, O. J. Lee, T. J. Gudmundsen, D. C. Ralph, and R. A. Buhrman, "Current-induced switching of perpendicularly magnetized magnetic layers using spin torque from the spin Hall effect," *Phys. Rev. Lett.* **109**, 096602 (2012).
- ⁶M. Weiler, A. Brandlmaier, S. Geprägs, M. Althammer, M. Opel, C. Bihler, H. Huebl, M. Brandt, R. Gross, and S. Goennenwein, "Voltage controlled inversion of magnetic anisotropy in a ferromagnetic thin film at room temperature," *New J. Phys.* **11**, 013021 (2009).
- ⁷A. Brandlmaier, S. Geprägs, G. Woltersdorf, R. Gross, and S. Goennenwein, "Nonvolatile, reversible electric-field controlled switching of remanent magnetization in multifunctional ferromagnetic/ferroelectric hybrids," *J. Appl. Phys.* **110**, 043913 (2011).
- ⁸N. A. Spaldin and M. Fiebig, "The renaissance of magnetoelectric multiferroics," *Science* **309**, 391–392 (2005).
- ⁹L. Martin and R. Ramesh, "Multiferroic and magnetoelectric heterostructures," *Acta Mater.* **60**, 2449–2470 (2012).
- ¹⁰L. Dreher, M. Weiler, M. Pernpeintner, H. Huebl, R. Gross, M. S. Brandt, and S. T. B. Goennenwein, "Surface acoustic wave driven ferromagnetic resonance in nickel thin films: Theory and experiment," *Phys. Rev. B* **86**, 134415 (2012).
- ¹¹M. Weiler, L. Dreher, C. Heeg, H. Huebl, R. Gross, M. S. Brandt, and S. T. B. Goennenwein, "Elastically driven ferromagnetic resonance in nickel thin films," *Phys. Rev. Lett.* **106**, 117601 (2011).
- ¹²P. G. Gowtham, T. Moriyama, D. C. Ralph, and R. A. Buhrman, "Traveling surface spin-wave resonance spectroscopy using surface acoustic waves," *J. Appl. Phys.* **118**, 233910 (2015).
- ¹³C. Chang, R. Tammimg, T. Broomhall, J. Janusonis, P. Fry, R. Tobey, and T. Hayward, "Selective excitation of localized spin-wave modes by optically pumped surface acoustic waves," *Phys. Rev. Appl.* **10**, 034068 (2018).

- ¹⁴C. A. Grimes, S. C. Roy, S. Rani, and Q. Cai, "Theory, instrumentation and applications of magnetoelastic resonance sensors: A review," *Sensors* **11**, 2809–2844 (2011).
- ¹⁵M. A. W. Schoen, D. Thonig, M. L. Schneider, T. J. Silva, H. T. Nembach, O. Eriksson, O. Karis, and J. M. Shaw, "Ultra-low magnetic damping of a metallic ferromagnet," *Nat. Phys.* **12**, 839–842 (2016).
- ¹⁶M. A. W. Schoen, J. Lucassen, H. T. Nembach, T. J. Silva, B. Koopmans, C. H. Back, and J. M. Shaw, "Magnetic properties of ultrathin 3d transition-metal binary alloys. I. spin and orbital moments, anisotropy, and confirmation of Slater-Pauling behavior," *Phys. Rev. B* **95**, 134410 (2017).
- ¹⁷L. Flacke, L. Liensberger, M. Althammer, H. Huebl, S. Geprägs, K. Schultheiss, A. Buzdakov, T. Hula, H. Schultheiss, E. R. J. Edwards, H. T. Nembach, J. M. Shaw, R. Gross, and M. Weiler, "New spin-wave propagation length scales in low damping metallic ferromagnets," e-print arxiv.org/abs/1904.11321v1.
- ¹⁸M. Collet, O. Gladii, M. Evelt, V. Bessonov, L. Soumah, P. Bortolotti, S. Demokritov, Y. Henry, V. Cros, and M. Bailleul *et al.*, "Spin-wave propagation in ultra-thin YIG based waveguides," *Appl. Phys. Lett.* **110**, 092408 (2017).
- ¹⁹R. C. Hall, "Single crystal anisotropy and magnetostriction constants of several ferromagnetic materials including alloys of NiFe, SiFe, AlFe, CoNi and CoFe," *J. Appl. Phys.* **30**, 1 (1959).
- ²⁰D. Hunter, W. Osborn, K. Wang, N. Kazantseva, J. Hattrick-Simpers, R. Suchoski, R. Takahashi, M. L. Young, A. Mehta, L. A. Bendersky, S. E. Lofland, M. Wuttig, and I. Takeuchi, "Giant magnetostriction in annealed Co_{1-x}Fe_x thin-films," *Nat. Commun.* **2**, 518 (2011).
- ²¹E. Quandt and A. Ludwig, "Giant magnetostrictive multilayers," *J. Appl. Phys.* **85**, 6232–6237 (1999).
- ²²E. Quandt and A. Ludwig, "Magnetostrictive actuation in microsystems," *Sens. Actuators A Phys.* **81**, 275–280 (2000).
- ²³E. Quandt, A. Ludwig, D. Lord, and C. Faunce, "Magnetic properties and microstructure of giant magnetostrictive TbFe/FeCo multilayers," *J. Appl. Phys.* **83**, 7267–7269 (1998).
- ²⁴A. Ludwig, M. Tewes, S. Glasmachers, M. Löhndorf, and E. Quandt, "High-frequency magnetoelastic materials for remote-interrogated stress sensors," *J. Magn. Magn. Mater.* **242**, 1126–1131 (2002).
- ²⁵H. D. Chopra, M. R. Sullivan, A. Ludwig, and E. Quandt, "Magnetoelastic and magnetostatic interactions in exchange-spring multilayers," *Phys. Rev. B* **72**, 054415 (2005).
- ²⁶F. Johnson, H. Garmestani, S. Chu, M. McHenry, and D. Laughlin, "Induced anisotropy in FeCo-based nanocrystalline ferromagnetic alloys (HITPERM) by very high field annealing," *IEEE Trans. Magn.* **40**, 2697–2699 (2004).
- ²⁷M. Cooke, M. Gibbs, and R. Pettifer, "Sputter deposition of compositional gradient magnetostrictive FeCo based thin films," *J. Magn. Magn. Mater.* **237**, 175–180 (2001).
- ²⁸M. Cooke, L. Wang, R. Watts, R. Zuberek, G. Heydon, W. Rainforth, and G. Gehring, "The effect of thermal treatment, composition and substrate on the texture and magnetic properties of FeCo thin films," *J. Phys. D Appl. Phys.* **33**, 1450 (2000).
- ²⁹R. Żuberek, A. Wawro, H. Szymczak, A. Wisniewski, W. Paszkowicz, and M. Gibbs, "Magnetostriction and magnetic anisotropy of FeCo/Au multilayers," *J. Magn. Magn. Mater.* **214**, 155–158 (2000).
- ³⁰C.-Y. Hung, M. Mao, S. Funada, T. Schneider, L. Miloslavsky, M. Miller, C. Qian, and H. Tong, "Magnetic properties of ultrathin NiFe and CoFe films," *J. Appl. Phys.* **87**, 6618–6620 (2000).
- ³¹Y. Cheng, A. J. Lee, J. T. Brangham, S. P. White, W. T. Ruane, P. C. Hammel, and F. Yang, "Thickness and angular dependent ferromagnetic resonance of ultra-low damping Co₂₅Fe₇₅ epitaxial films," *Appl. Phys. Lett.* **113**, 262403 (2018).
- ³²M. Pernpeintner, R. B. Holländer, M. J. Seitner, E. M. Weig, R. Gross, S. T. B. Goennenwein, and H. Huebl, "A versatile platform for magnetostriction measurements in thin films," *J. Appl. Phys.* **119**, 093901 (2016).
- ³³S. Timoshenko, W. Weaver, and D. Young, *Vibration Problems in Engineering*, 5th ed. (John Wiley and Sons, New York, 1990).
- ³⁴S. S. Verbridge, J. M. Parpia, R. B. Reichenbach, L. M. Bellan, and H. G. Craighead, "High quality factor resonance at room temperature with nanostrings under high tensile stress," *J. Appl. Phys.* **99**, 124304 (2006).

- ³⁵R. Gross and A. Marx, *Festkörperphysik* (De Gruyter Oldenbourg, 2012).
- ³⁶S. Chikazumi, *Physics of Ferromagnetism*, International Series of Monographs on Physics (Clarendon Press, 1997).
- ³⁷An active calibration of the mechanical amplitude was not possible with this sample. The mechanical amplitude was estimated using geometrically similar samples from pre-stressed SiN and pre-stressed Al.
- ³⁸M. J. Seitner, K. Gajo, and E. M. Weig, "Damping of metallized bilayer nanomechanical resonators at room temperature," *Appl. Phys. Lett.* **105**, 213101 (2014).
- ³⁹F. Hoehne, Y. A. Pashkin, O. Astafiev, L. Faoro, L. Ioffe, Y. Nakamura, and J. Tsai, "Damping in high-frequency metallic nanomechanical resonators," *Phys. Rev. B* **81**, 184112 (2010).
- ⁴⁰F. Cardarelli, "Ferrous metals and their alloys," in *Materials Handbook: A Concise Desktop Reference* (Springer, New York, 2018), pp. 101–248.
- ⁴¹E. R. Edwards, H. T. Nembach, and J. M. Shaw, "Co₂5Fe₇5 thin films with ultralow total damping of ferromagnetic resonance," *Phys. Rev. Appl.* **11**, 054036 (2019).
- ⁴²M. Pernpeintner, "Nanomechanical Hybrid Systems," Ph.D. thesis (Technical University of Munich, 2016).
- ⁴³A. N. Cleland, *Foundations of Nanomechanics: From Solid-state Theory to Device Applications* (Springer Science & Business Media, 2003).
- ⁴⁴J. Davis, D. Vick, D. Fortin, J. Burgess, W. Hiebert, and M. Freeman, "Nanotorsional resonator torque magnetometry," *Appl. Phys. Lett.* **96**, 072513 (2010).
- ⁴⁵F. Jiménez-Villacorta, A. Espinosa, E. Céspedes, and C. Prieto, "Magnetic properties and short-range structure analysis of granular cobalt silicon nitride multilayers," *J. Appl. Phys.* **110**, 113909 (2011).
- ⁴⁶S. S. Kalarickal, P. Krivosik, M. Wu, C. E. Patton, M. L. Schneider, P. Kabos, T. J. Silva, and J. P. Nibarger, "Ferromagnetic resonance linewidth in metallic thin films: Comparison of measurement methods," *J. Appl. Phys.* **99**, 093909 (2006).
- ⁴⁷R. Ohshima, S. Klingler, S. Dushenko, Y. Ando, M. Weiler, H. Huebl, T. Shinjo, S. T. Goennenwein, and M. Shiraishi, "Spin injection into silicon detected by broadband ferromagnetic resonance spectroscopy," *Appl. Phys. Lett.* **110**, 182402 (2017).